Energy Storage Materials 28 (2020) 325–333

Contents lists available at ScienceDirect

Energy Storage Materials

journal homepage: www.elsevier.com/locate/ensm

Totally compatible P_4S_{10+n} cathodes with self-generated Li^+ pathways for sulfide-based all-solid-state batteries

Xiaona Li [a,1], Jianwen Liang [a,1], Mohammad Norouzi Banis [a], Jing Luo [a], Changhong Wang [a], Weihan Li [a], Xia Li [a], Qian Sun [a], Yongfeng Hu [b], Qunfeng Xiao [b], Tsun-Kong Sham [c], Li Zhang [d], Shangqian Zhao [d], Shigang Lu [d], Huan Huang [e], Ruying Li [a], Xueliang Sun [a,*]

[a] Department of Mechanical and Materials Engineering, University of Western Ontario, 1151 Richmond St, London, Ontario, N6A 3K7, Canada
[b] Canadian Light Source, 44 Innovation Boulevard, Saskatoon, SK, S7N 2V3, Canada
[c] Department Chemistry, University of Western Ontario, 1151 Richmond St, London, Ontario, N6A 3K7, Canada
[d] China Automotive Battery Research Institute Co. Ltd, 5th Floor, No. 43, Mining Building, North Sanhuan Middle Road, Beijing, 100088, China
[e] Glabat Solid-State Battery Inc., 700 Collip Circle, London, ON, N6G 4X8, Canada

ARTICLE INFO

Keywords:
All-solid-state battery
Sulfide electrolyte
Phosphorus sulfide molecule
Interfacial
Ionic conductivity

ABSTRACT

All-solid-state lithium sulfur batteries (ASSLSBs) are considered promising candidates for next-generation energy-storage systems due to their enhanced safety and high theoretical energy density. However, usually both solid-state electrolyte (SSE) and conductive carbon need to be incorporated into the cathode composite to provide Li^+/electron pathways, leading to the reduced energy density and inevitable SSE decomposition. Moreover, the real electrochemical behavior of S or Li_2S cathodes can not be reflected due to the partially overlapped redox reaction of SSE. Herein, a series of unique P_4S_{10+n} cathodes for high-performance ASSLSBs that totally do not need any extra SSE additives are reported. Synchrotron-based X-ray absorption near edge structure coupled with other analyses confirmed that ionic conductive Li_3PS_4 together with $Li_4P_2S_6$ components can be electrochemically self-generated during lithiation process and partially maintained to provide fast Li^+ transport pathways within the cathode layer. This is further evidenced by a 30–43-fold higher reversible capacity for P_4S_{10+n}/C cathodes compared to a S/C cathode. Bulk-type ASSLSBs based on the P_4S_{34}/C cathode show a highly reversible capacity of 883 mAh g^{-1} and stable cycling performance over 180 cycles with a high active material content of 70 wt%. The present study provides a promising approach for generating ionic conductive components from the electrode itself to facilitate Li^+ migration within electrodes in ASSLSBs.

1. Introduction

All-solid-state lithium batteries have received enormous attention due to safety considerations and promise to realize both high energy and high power densities [1,2]. Significant progress is achieved because of the great improvement of sulfide-based solid-state electrolytes (SSEs) with superionic conductivity approaching that of liquid electrolytes [1, 3–6]. Using sulfur (S) or Li_2S as an active cathode material to achieve all-solid-state lithium-sulfur batteries (ASSLSBs) has gained extensive attention due to the high theoretical capacity of 1675 and 1167 mAh g^{-1} for S and Li_2S, respectively [7]. More importantly, the well-known shuttling effects caused by the polysulfide intermediates can be radically avoided based on solid-phase Li–S redox reaction in ASSLSBs system.

However, SSEs and conductive carbon are usually indispensable components besides S (or Li_2S) active material within the cathode composites, which raises several drawbacks for ASSLSBs. Firstly, the narrow electrochemical stability window of sulfide SSEs (such as 1.71–2.31 V for Li_3PS_4, 1.72–2.29 V $Li_{10}GeP_2S_{12}$, vs. Li/Li^+) [8] causes SSEs decomposition in the applied voltage for ASSLSBs (usually 1.0–3.0 V vs. Li/Li^+), especially with the existence of a large amount of carbon additives. Thus, the electrochemical behavior of ASSLSBs are not only attributed to the electrochemical reaction of S (or Li_2S), but also overlapped with the sulfide SSEs redox (S^{2-}/S) reaction during cycling. The real electrochemical behavior of S (or Li_2S) is actually not reflected, particularly the calculations of the reversible capacity and S (or Li_2S) utilization since the

* Corresponding author.
E-mail address: xsun9@uwo.ca (X. Sun).
[1] The authors contribute equally to this work.

https://doi.org/10.1016/j.ensm.2020.03.014
Received 5 February 2020; Received in revised form 11 March 2020; Accepted 12 March 2020
Available online 19 March 2020

partial capacity-contribution of sulfide SSEs. Indeed, capacities higher than the theoretical capacity of S (or Li_2S) in sulfide SSE-based ASSLSBs have been previously reported [9–11]. Secondly, because of the limited solid-solid contact among the S (or Li_2S), carbon, and SSE, huge interfacial resistance which leads to low active material utilization and sluggish reaction kinetics, is still a big challenge for ASSLSBs. The interfacial Li^+ transport within the cathode composites layer is several orders of magnitude lower than the Li^+ transport within the SSE layer [12]. Thirdly, the addition of a large amount of electrochemically inactive components significantly lowers the energy density of ASSLSBs. Due to the quite poor ionic/electronic conductivities of S (electronic conductivity of 5×10^{-30} S cm^{-1}) [13] and Li_2S (electronic conductivity of $\sim 10^{-13}$ S cm^{-1}, ionic conductivity of $\sim 10^{-9}$ S cm^{-1}) [14], significant amounts of SSE and carbon have to be added to ensure Li^+/e^- migration, which compromises the active material contents within the cathode composites. As a result, the S or Li_2S contents are usually much low in reported ASSLSBs, which are around 13–50 wt% [7,11,14–25], even below 10 wt% in some cases [10,26], leading to dramatically reduced energy density.

Recently, the emergence of some unique electrode materials sheds light on the design of simplified ASSLSBs, reflecting the real electrochemical behavior of active material and eliminating the influence of decomposition of SSEs. For instance, taking advantage of the mixed conductive property of $LiTiS_2$ (electronic conductivity over 1 S cm^{-1}, and Li^+ self-diffusion coefficient of $\sim 1 \times 10^{-9}$ cm^2 s^{-1}) [27,28], $LiTiS_2$ itself was demonstrated to provide both electronic and ionic pathways. Thus, $LiTiS_2$ alone can be used individually as a cathode material in all-solid-state pseudocapacitor system [29]. Similarly, amorphous $LiCoO_2$-Li_xMO_y [30] and $Na_{0.7}CoO_2$-Na_xMO_y [31] (M = N, S, P, B, or C) materials can also be directly used as cathode materials without any SSE additives in all-solid-state batteries. Evidently, simplifying traditional S (or Li_2S)/SSE/C cathode composites design to binary or even individual component by internally forming a highly homogeneous ionic/electronic conductive network is an effective strategy to develop high-performance ASSLSBs and provide actual electrochemical information of targeted active materials.

Sulfur-rich phosphorus sulfide molecules (P_4S_{10+n}, n = 6, 12, 18, 24, and 30) are a new family of P–S molecules proposed and synthesized by our group with higher S/P molar ratio than traditional P_4S_{10}; additional S can be inserted into the six P–S–P bonds in tetrahedral P_4S_{10} matrix [32]. Herein, we demonstrate the development of a series of high-capacity P_4S_{10+n}/C cathode with a unique electrochemical self-activation process in ASSLSBs. The most striking feature is that no SSE components are needed in cathode composites since highly ionic conductive Li–P–S species can be self-generated during the lithiation process together with reduced S species (Fig. 1a). Synchrotron-based P and S K-edge X-ray

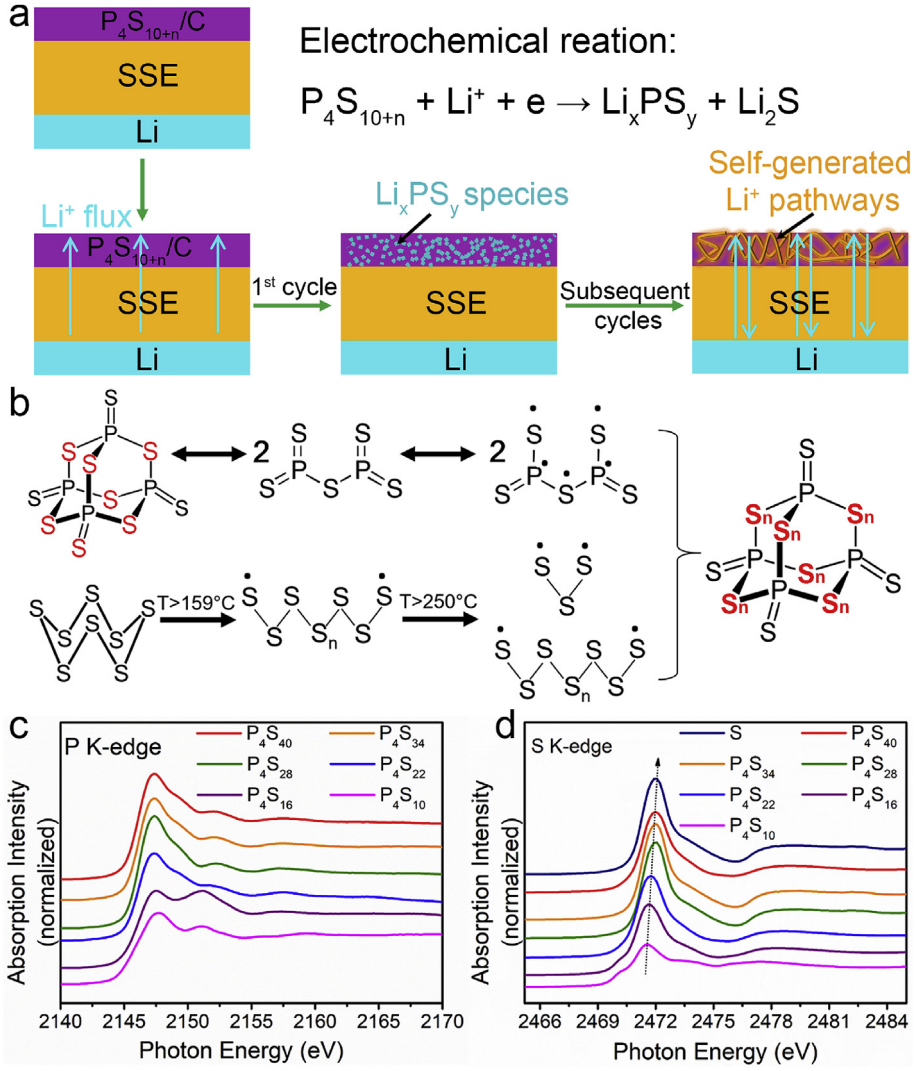

Fig. 1. (a) Schematics for the proposed mechanism of P_4S_{10+n}/C cathode in ASSLSBs. (b) A schematic illustration of the synthesize route for P_4S_{10+n} molecules. (c) Normalized P K-edge XANES spectra of the as-prepared P_4S_{10+n} samples and commercial dimer P_4S_{10}. (d) Normalized S K-edge XANES spectra of as-prepared P_4S_{10+n} samples in comparison with commercial S and P_4S_{10}.

absorption near edge structure (XANES), Raman and X-ray photoelectron spectroscopy (XPS) analyses revealed the transformation of the insulating P_4S_{16} to highly ionic conductive Li_3PS_4 (together with a small amount of $Li_4P_2S_6$ species with lower ionic conductivity) during the initial lithiation process. Those ionic conductive Li–P–S species also partially participate in a highly reversible redox process during lithiation/delithiation, while still can provide fast Li^+ migration pathways within the cathode layer. The incorporation of P_4S_{10+n}/C cathodes significantly improves the reversibility compared to the bare S/C in ASSLSBs, exhibiting the reversible capacity of 30–43-fold higher than a S/C cathode. A high reversible capacity of 883 mAh g^{-1} and a high active material content of 70 wt% are achieved for bulk-type ASSLSBs based on the P_4S_{34}/C cathode, which are among the best performance of the state-of-the-art of ASSLSBs. These results prove the substantial improvement in the interfacial properties due to the self-generated homogeneous ionic conductive components, which enabled the excellent electrochemical performance of the ASSLSBs.

2. Results and discussion

The P_4S_{10+n} (n = 6, 12, 18, 24, 30) molecules were prepared from elemental S (S_8) and commercial P_2S_5 (i.e. dimer P_4S_{10}) based on our previous report (see Methods for details) [32]. Basically, in the co-melt system, the S_8 ring is opened to a polysulfide chain or cracked polysulfides with diradical chain ends, and P_4S_{10} converts into P_2S_5 radical. Thus, an additive reaction readily happens between these two components, with additional S inserted into the P–S–P bonds of the pristine P_4S_{10} structure form P–S_n–P bonds (as shown in Fig. 1b) [32]. X-ray diffraction (XRD, Fig. S1) analysis reveals their amorphous structures similar to those reported previously [32].

X-ray absorption spectroscopy (XAS) was employed at the S and P K-edge in total electron yield (TEY) mode to confirm the chemical state of the P_4S_{10+n} samples. It should be noted that in P_4S_{10}, there are four equivalent P sites and two sets of S sites with the four terminal S atoms involved in P═S bonding showing π characteristic. The normalized P K-edge X-ray absorption near-edge structure (XANES) spectra of P_4S_{10+n} samples are compared to the standard sample of comercial P_2S_5 (i.e. P_4S_{10}) in Fig. 1c. All XANES spectra display a dominant feature centered at 2147.3 eV, which can be attributed to the P 1s core level transition to antibonding t2* state [33]. Meanwhile, additional broad feature at higher energy around 2152 eV might be related to the influence of different amount of sulfur atoms within the six P–S_n–P bonds (multiple scattering) [34] or possible oxidation of phosphorous [35]. In the S K-edge spectra of the P_4S_{10+n} samples presented here (Fig. 1d), the peak maximum of the primary absorption feature (i.e., the absorption edge) is found between 2471.4 eV for P_4S_{10} and 2472.2 eV for commercial S, corresponding to the occupied S 1s orbitals transition to unoccupied S 3p s* antibonding orbitals [36]. There is a small shoulder at ~ 2471 eV due to π* transitions. Notably, the absorption edge of the synthesized P_4S_{10+n} samples slightly shifted to higher energy accompanied by an increase in whiteline intensity with the increasing sulfur content in the amorphous molecules. This indicates charge depletion relative to P_4S_{10} but still lower than commercial S.

The as-prepared P_4S_{10+n} molecules present a large particle size of several microns in diameter [32]; however, taking the advantage of good solubility of P_4S_{10+n} molecules in diethylene glycol dimethyl ether (DEGDME), the P_4S_{10+n}/C cathode composites can be prepared by a solution method to achieve better homogeneity and smaller particle size. Each P_4S_{10+n} sample was dissolved in DEGDME (Fig. S2), and followed by addition of an appropriate amount of acetylene black. The solution was stirred for 24 h and subsequently dried at 200 °C under vacuum to evaporate the DEGDME. Field emission scanning electron microscopic (FE-SEM) images of typical P_4S_{16}/C composite are shown in Fig. S3 with a particle size around 50 nm. The P, S, and C elements showed a uniform distribution (Fig. S4). The P_4S_{10+n}/C composites were used directly as cathodes in sulfide-based ASSLSBs without any solid electrolyte additives into the cathode.

The discharge-charge curves of the initial five cycles for the ASSLSBs with P_4S_{16}/C are shown in Fig. 2a. The specific capacity was normalized by the weight of P_4S_{16} in the cathode composite. The P_4S_{16}/C cathode exhibited initial discharge and charge capacities of ~713 and 620 mAh g^{-1}, respectively. As presented in Fig. 2a, in the first discharge process, two remarkable discharge plateaus at 2.2 V and 1.3 V are detected. Meanwhile, one charge plateau at 2.3 V is observed during the first charge process. In subsequent cycles, the charge plateaus remain stable, while the main discharge plateau at 2.2 V splits into two plateaus at 2.3 and 2.05 V, respectively, and the position of another discharge plateau at 1.3 V also remains unchanged. Corresponding cyclic voltammogram (CV) curves of the P_4S_{16}/C composite in a potential range from 1.0 to 3.0 V vs. Li/Li^+ at a scan rate of 0.05 mV s^{-1} are presented in Fig. S5. The reversible capacity of the P_4S_{16}/C cathode remained about 467 mAh g^{-1} after 100 cycles (Fig. 2b). Comparatively, even though the S/C cathode exhibited an initial discharge capacity of 465 mAh g^{-1}, there was barely any reversible capacity (~20 mAh g^{-1}) in the following cycles under the same operating conditions (Fig. 2c). Obviously, the low reversible capacity of the S/C cathode is due to the lack of Li^+ migration pathway within the cathode considering the low ionic conductivity of both sulfur and lithium sulfide [9,13,14]. Moreover, the galvanostatic intermittent titration technique (GITT) was employed to reveal the polarization and corresponding Li^+ self-diffusion coefficient (D_{Li}) of the P_4S_{16}/C cathode (Fig. 2d). The polarizations mostly deviated no more than 0.25 V (Fig. S6), indicating a feasible electrochemical reaction. The reaction-voltage-dependent D_{Li} calculated from the GITT curves were in the magnitude ranging from 10^{-11} to 4×10^{-10} cm^2 s^{-1}. Basically, the D_{Li} values are high enough for the conversion reaction of P_4S_{16}/C without the addition of any solid electrolyte [37]. As illustrated in Fig. 2e and f, compared to the S/C cathode, feasible Li^+ migration pathways are inherent in the P_4S_{16}/C cathode, ensuring reversible lithiation and delithiation in ASSLSBs.

To investigate the structural evolution of P_4S_{16}/C cathode during lithiation and delithiation process, Raman analysis was firstly conducted. Fig. 3a shows the *ex-situ* Raman spectra of the P_4S_{16}/C cathode at different states of discharge or charge. For the pristine P_4S_{16} molecule, the peak at 126 cm^{-1} was due to the P═S bonds; the peaks at 189, 263, 300, 372, and 410 cm^{-1} were assigned to the P–S bonds; and the other labeled peaks could be attributed to the symmetry species of the S–S bonds [32]. After mixed with acetylene black by solution method, the P–S related peaks are weakened due to the presence of acetylene black in the composite, but the main characteristic peaks are remained (Fig. S7). Typical Raman spectrum of the commercial Li_3PS_4 exhibited two peaks at 290 and 420 cm^{-1} attributing to the PS_4^{3-} structural unit based on previous reports [38,39]. During the initial discharge to 1.8 V, all peaks related to P═S and P–S bonds in the Raman spectra disappeared, remaining three typical peaks for S–S bonds at 148, 216, and 476 cm^{-1}. Upon further lithation (discharged to 1.4 V), the intensity of S–S peaks at 216 and 476 cm^{-1} significantly reduced, accompanied by the appearance of a new weak peak at around 290 cm^{-1} due to the PS_4^{3-} unit. At the fully discharged state (1.0 V), a strong peak at 420 cm^{-1} also typically for the PS_4^{3-} unit was observed [38]; the small peak at 380 cm^{-1} was correspondent to the $P_2S_6^{4-}$ anion reported at 382 cm^{-1} [40]. As a conclusion, the local structure of P_4S_{16} molecule after the initial discharge process was totally changed, presumably forming Li_xPS_4 with PS_4^{3-} species similar to the Li_3PS_4 electrolyte together with a small amount of $P_2S_6^{4-}$ species. Upon delithiation (recharged to 2.7 V), the peaks assigned to the PS_4^{3-} and $P_2S_6^{4-}$ species completely disappeared, and the peaks related to S–S bonds at 148, 216, and 476 cm^{-1} reappeared. Further recharged to 3.0 V, the P–S characteristic peak subsequently reappeared. No peaks due to P═S bonds were observed, indicating that the local structure of cathode after the first lithiation/delithiation cycle was different from the initial P_4S_{16} molecule.

P K-edge and S K-edge XANES measurements of the P_4S_{16}/C cathode at different discharge/charge states were further conducted to reveal the

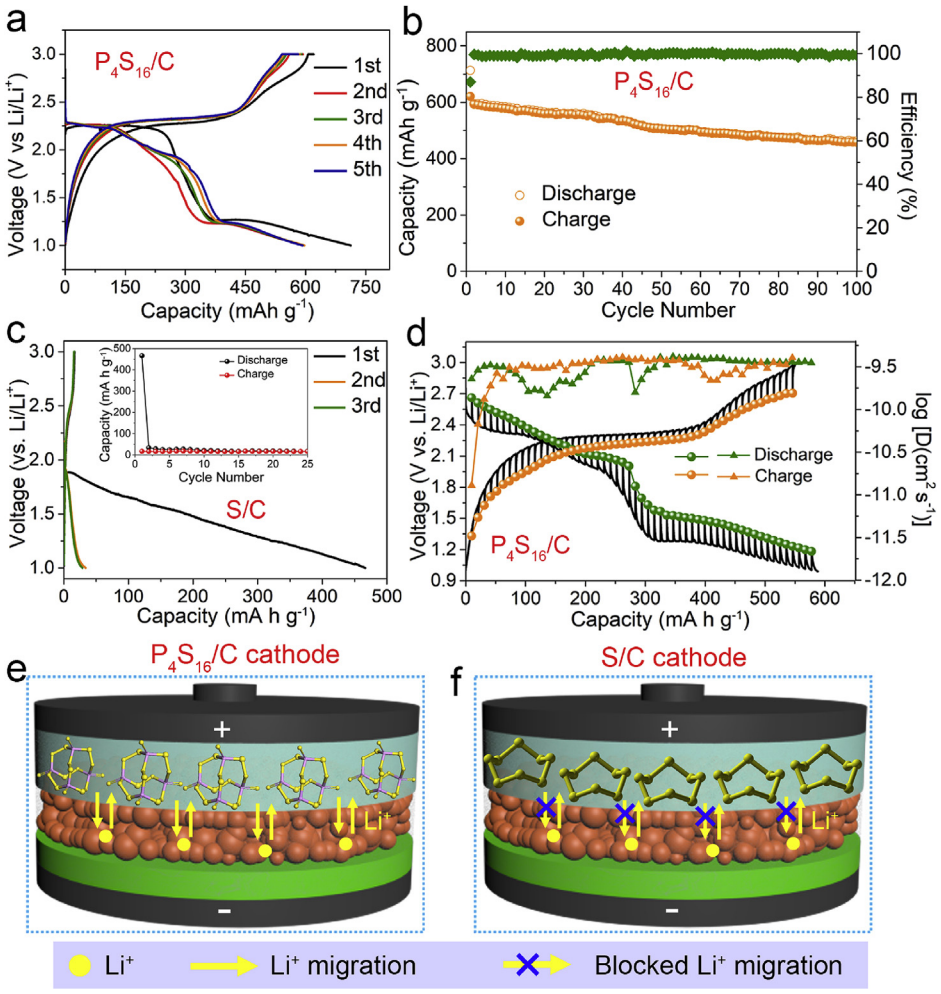

Fig. 2. (a) Discharge-charge curves of ASSLB with P_4S_{16}/C cathode at 20 mA g^{-1}. (b) Cycling performance of P_4S_{16}/C cathode at 100 mA g^{-1} (with initial 5 cycles at 20 mA g^{-1}). (c) Discharge-charge curves and cycling performance (insert) of ASSLB with S/C cathode at 20 mA g^{-1}. (d) Transient discharge/charge voltage profiles and calculated diffusion coefficients of P_4S_{16}/C cathode at 20 mA g^{-1}. Schematic ion transport in ASSLSBs with (e) P_4S_{16}/C and (f) S/C cathodes.

lithiation/delithiation effects on the atomic structure and composition of P_4S_{16} (Fig. 3b). The spectra of P_4S_{16}, commercial Li_3PS_4, S and Li_2S are presented for comparison. In the P K-edge spectra, different from the spectra of those as-prepared P_4S_{10+n} samples, a pronounced feature with slightly higher energy at 2148.0 eV was observed for the P_4S_{16}/C electrodes at different states of lithiation and delithiation [33]. This feature was consistent well with the spectrum of the commercial Li_3PS_4 and reported lithium thiophosphates [33,38], indicating a similar electronic state of P element within these species. Surprisingly, an additional feature at a lower energy of 2144.8 eV was observed for the P_4S_{16}/C cathode when discharged to 1.0 V and recharged to 2.3 V, but this feature was absent from other discharge/charge states or the synthesized P_4S_{10+n} samples (Fig. 3b). This feature is neither reported for any synthesized lithium thiophosphates glass or ceramic with various amounts of Li_2S and P_2S_5 [41], while the similar signal was reported for the computational XANES spectra of Li_2PS_3 ($Li_4P_2S_6$) [42]. The results are consistent well with the *ex-situ* Raman analysis regarding the evidence of $P_2S_6^{4-}$ anion when discharge to 1.0 V and re-charged to 2.3 V. This is reasonable based on previous reports about the possible conversion between Li_3PS_4 and $Li_4P_2S_6$ [43,44]. As presented in Fig. 3c, the PS_4^{3-} and $P_2S_6^{4-}$ units exhibit different anion polyhedra. The PS_4^{3-} unit shows PS_4^{3-} tetrahedra with a central P atom surrounded by four S atoms equally sharing the negative charge of three electrons; the $P_2S_6^{4-}$ unit is actually a dimer with two PS_3^{2-} linked by a P–P bond, where the negative net charge of four electrons is distributed equally among the six S atoms. The relatively different bonding environments could induce changes in the ground state charge density around P, leading to the distinct signal of the P K-edge spectra.

Corresponding S K-edge spectra were presented in Fig. 3b. Obviously, the peak of the S K-edge shifted to lower energy during discharge and gradually returned to the original energy during charge. The S component of the P_4S_{16}/C cathode participated in the reversible redox reactions without generating radical polysulfides or lithium sulfides at the fully discharges, differentiating from the reference commercial Li_3PS_4 spectrum. There should be features related to the $P_2S_6^{4-}$ unit as well, however, the XANES characteristics for the PS_4^{3-} and $P_2S_6^{4-}$ units are too similar to practically distinguish them. The P–S bonding in the two anion units is very similar. After recharged to 3.0 V, the signals of S K-edge are located between S and pristine P_4S_{16} (Fig. 3b and Fig. S8), indicating a high reversibility of the cathode.

X-ray photoelectron spectroscopy (XPS) further revealed the chemistries of the P and S atoms in the P_4S_{16}/C electrode during the first discharge/charge cycle (Fig. 4). The XPS spectrum of the commercial Li_3PS_4 is shown as a reference. On the S 2p XPS spectra, two main groups with S $2p_{3/2}$ centered at 163.5 (bridging S: P–S_n–P) and 162 (non-bridging S: P═S) eV were observed during the discharge/charge process. The intensity of the doublet peaks at lower binding energy (S $2p_{3/2}$ at 162 eV, green shading) increased during the discharging (lithiation) process and decreased during the charging (delithiation) process. An opposite trend was observed for the peaks at higher binding energy (S $2p_{3/2}$ at 163.5 eV, yellow shading). The locations and integral area ratios

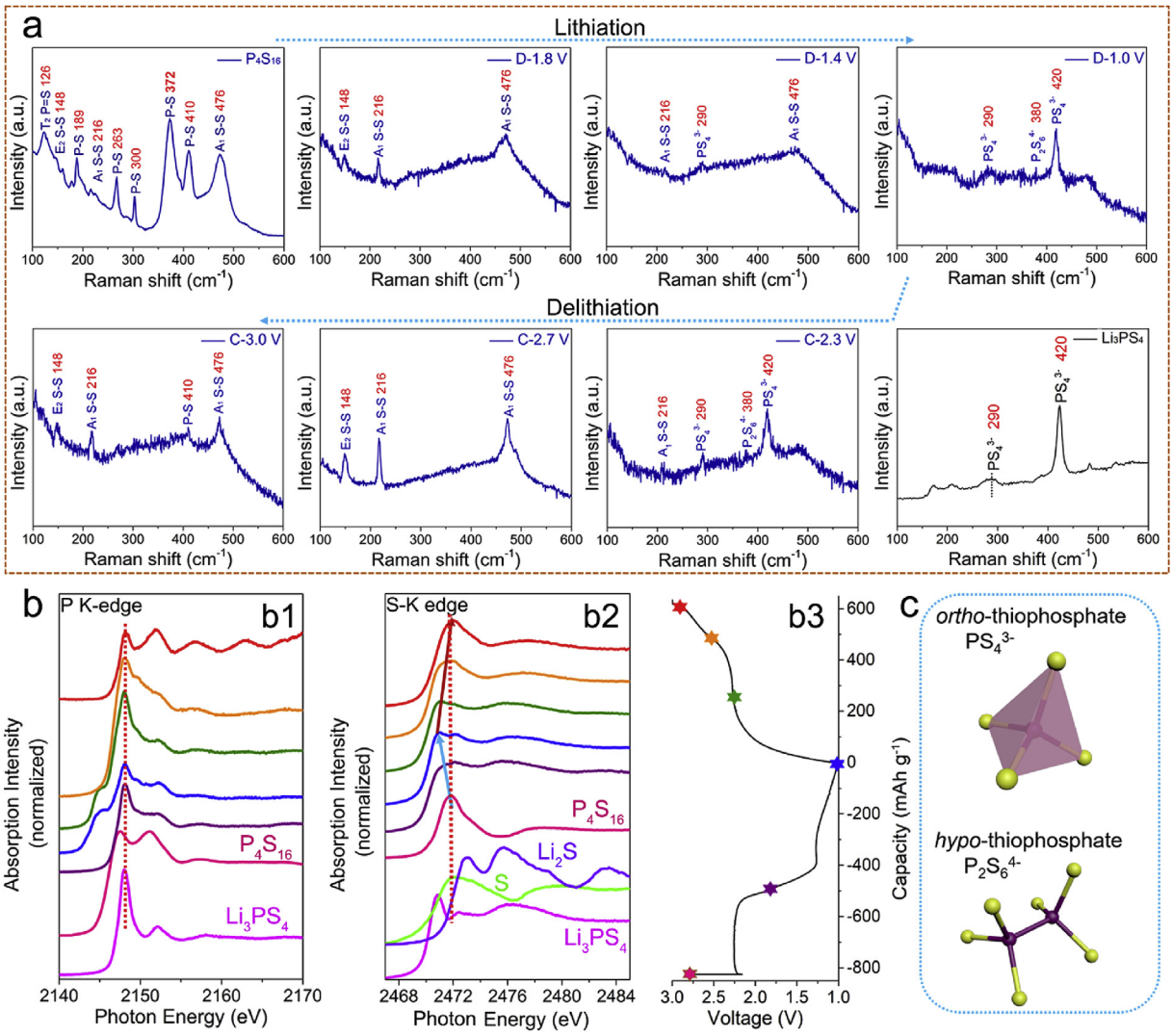

Fig. 3. Understanding the reaction mechanism of P_4S_{16}/C cathode. *Ex-situ* (a) Raman and (b) XANES analysis on P_4S_{16}/C cathodes at different discharge/charge states from ASSLSBs. P K-edge and S K-edge XANES spectra of P_4S_{16}/C cathodes were collected at 1.8, 1.4, and 1.0 V of discharge and 2.3, 2.7, and 3.0 V of re-charge. The colors of the spectra are corresponding to the labels on the discharge-charge curve. (c) Typical anion species of thiophosphates with PS_4^{3-} and $P_2S_6^{4-}$ polyhedra and the underlying bonding situation. (For interpretation of the references to color in this figure legend, the reader is referred to the Web version of this article.)

of these peaks are compared in Table S1. Despite of the trends of peak intensities, the two sets of peaks shifted to lower binding energies during discharge (reduction process of S species) and returned higher binding energies during charge (oxidation process of S species), which is consistent well with the XANES data. Moreover, the S species at low binding energy shifted to 161.4 eV at the fully discharged state, which is very similar to the spectrum commercial Li_3PS_4; no signal for electron-rich S species such as Li_2S (~159.8 eV) [44] was observed. Similar to the XANES analysis that the similar chemical environment of S in Li_3PS_4 and $Li_4P_2S_6$ makes it difficult to distinguish the two species by XPS. The area ratio of peaks from low to high binding energy increases from 0.3:1 for the fresh P_4S_{16} cathode to 3.9:1 after discharging to 1.0 V and decreased back to 1.2:1 after charging to 3.0 V. The higher content of S species at lower binding energy indicates that the *in-situ* formed ionic conductive Li–P–S species partially involved a redox process without fully oxidized. Generally, the evolution of the S 2p XPS spectra was quite similar to the reported anion electrochemistry of the thiophosphate electrolytes involving the reversible lithiation/delithiation of -P-S_x-P- species [38,44]. Based on *ex-situ* Raman, XANES, and XPS measurements, the lithiation process of P_4S_{16} involved with the formation of ionic conductive Li–P–S species (including the highly ionic conductive Li_3PS_4 together with a small amount of $Li_4P_2S_6$ species at the fully-lithiated state). The delithiation process is more likely involved with the re-formation of -P-S_n-P- species as well as the partial extraction of Li^+ in the ionic conductive Li–P–S species. In the subsequent cycles, the ionic conductive Li–P–S species also partially participated in the electrochemical reaction based on the electrochemical behavior of sulfide SSEs involving S_x^{2-}/S_x redox reaction as reported [45–47]. While the self-generated Li^+ migration pathways still can be maintained evidenced by the excellent cycling stability of P_4S_{16}/C in ASSLSBs without any SSE additives.

All-solid-state cells using other P_4S_{10+n}/C cathodes were also assembled to study the lithiation/delithiation properties. Similar to the P_4S_{16}/C cathode, all the other P_4S_{10+n}/C cathodes can also generate ionic conductive Li–P–S species with subtle variations after lithiation. With an increasing n value of P_4S_{10+n}/C cathodes (i.e. increasing of S content), the additional S component would convert to Li_2S after lithiation, based on the lithiation/delithiation behaviors of P_4S_{10+n}/C cathodes in liquid Li–S batteries [32]. The formation of Li_2S was proven by the XPS result of the fully lithiated P_4S_{28}/C cathode shown in Fig. S9. During the charge process, -P-S_n-P- species and partially delithiated ionic conductive Li–P–S species are assumed to be formed. Since the small amount of self-generated $Li_4P_2S_6$, the theoretical capacity of P_4S_{22}, P_4S_{28}, P_4S_{34}, and P_4S_{40} are calculated as 766, 946, 1061, and 1145 mAh g^{-1} respectively,

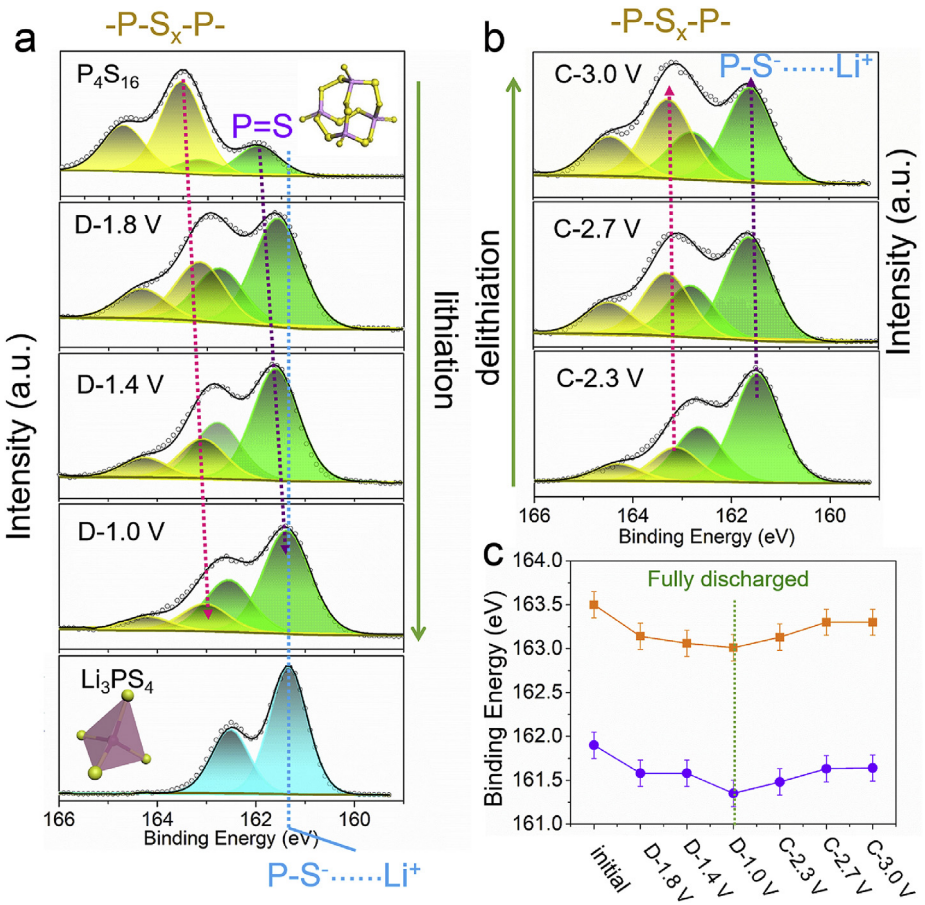

Fig. 4. *Ex-situ* X-ray photoelectron spectroscopy study on the P_4S_{16}/C cathode at different discharge/charge states in ASSLSBs. S 2p XPS spectra of P_4S_{16}/C cathode at different (a) discharge and (b) charge states were collected. (discharged to 1.8, 1.4, and 1.0 V, and re-charged to 2.3, 2.7, and 3.0 V). (c) The result of the peak fitting results of S $2p_{3/2}$ of P_4S_{16}/C cathode at different discharge/charge states.

assuming the fully-lithiated products were Li_3PS_4 and Li_2S; the molar ratios of the formed Li_3PS_4 and Li_2S are 4:6, 4:12, 4:18, and 4:24 in order. Correspondingly, when coupled with the Li anode, the theoretical energy densities of the Li/P_4S_{10+n} (n = 12, 18, 24, and 30) cells can be as high as 1400, 1595, 1754, and 1854 Wh Kg^{-1}, respectively.

The discharge-charge profiles of the four P_4S_{10+n}/C (P_4S_{22}/C, P_4S_{28}/C, P_4S_{34}/C, and P_4S_{40}/C) cathodes in ASSLSBs at the first two (20 mA g^{-1}), 5th (50 mA g^{-1}), 10th (100 mA g^{-1}) and 20th (200 mA g^{-1}) cycles

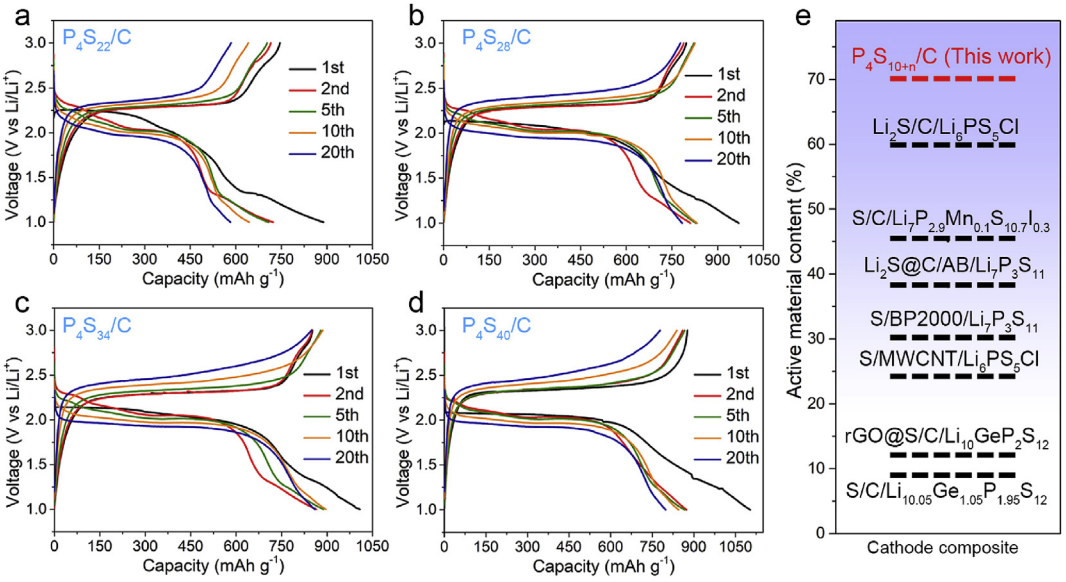

Fig. 5. (a–d) Discharge/charge profiles P_4S_{10+n}/C cathodes in sulfide ASSLSBs. Current density: 20 mA g^{-1} for the first two cycles, 50 mA g^{-1} for the 5th cycle, 100 mA g^{-1} for the 10th cycle, and 200 mA g^{-1} for the 20th cycle. (e) Summary of reported active material content within cathode composites in ASSLSBs [7,10,11,14–23,26].

are presented in Fig. 5a–d. The low current density in the initial few cycles was intended for the self-activation process. Noteworthy, all four P_4S_{10+n}/C cathodes delivered high initial Coulombic efficiencies (CEs) of 84%, 82%, 84%, and 79%, respectively for P_4S_{22}/C, P_4S_{28}/C, P_4S_{34}/C, and P_4S_{40}/C cathodes, with corresponding reversible capacities of 745, 797, 883, and 876 mAh g^{-1}. The relatively lower initial CE and reversible capacity of P_4S_{10+n}/C cathodes with the increasing of n number is reasonable due to the lower content of *in-situ* formed ionic conductive Li–P–S component. Since there was no additional solid electrolyte within the P_4S_{10+n}/C electrodes, the *in-situ* formed ionic conductive Li–P–S component played a key role in providing Li^+ pathways. Therefore, the electrochemical reactions would be sluggish and incomplete without sufficient Li^+ pathways. After the self-activation process at low current density during the initial few cycles, the P_4S_{10+n}/C electrodes exhibited comparable reversible capacities with slightly increased polarization when increasing the current densities as observed in the discharge-charge profiles (Fig. 5a–d). Furthermore, with a larger S content in P_4S_{10+n}/C, the discharge charge profiles become more similar to typical profiles involving redox reaction of S_x/S_x^{2-} in ASSLSBs. Taking advantages of those self-generated ionic conductive components, the active material content within the P_4S_{10+n}/C cathodes (i.e. P_4S_{10+n} here) are much higher than traditional S (or Li_2S)/C/SSE cathodes as compared in Fig. 5e [7,10,11,14–23,26].

To further understand the effect of S_x/S_x^{2-} redox on the electrochemical behavior and reversibility of the P_4S_{10+n}/C cathodes during cycling, dQ/dV curves of the P_4S_{10+n}/C cathodes in the first 20 cycles were plotted as shown in Fig. 6a–d. One dominant redox couple with an anodic peak centered at ~2.3 V and cathodic peak centered at ~2.0 V was observed for all the P_4S_{10+n}/C cathodes, corresponding to the typical redox reaction of S_x/S_x^{2-}. Furthermore, one or two small cathodic peaks at ~2.1 and ~2.2 V were as observed, which might be related to the formation of Li–P–S species and their partial redox behavior during cycling. It can also be seen that a high-voltage shift while low-voltage shift for anodic peak and cathodic peak with the increasing of cycling number, respectively. Such a phenomenon is more obvious with more sulfur content is P_4S_{10+n}/C cathodes, suggesting the limited amount of self-formation Li^+ migration pathways. The corresponding cycling stabilities, areal capacities, and the CEs of the four P_4S_{10+n}/C cathodes are presented in Fig. 6e and f. The ASSLSBs with P_4S_{22}/C, P_4S_{28}/C, P_4S_{34}/C, and P_4S_{40}/C cathodes showed good capacity retentions, with capacities of 559, 710, 797, and 688 mAh g^{-1}, respectively, after 50 cycles. Furthermore, the ASSLSBs with P_4S_{34}/C cathode exhibited stable cycling

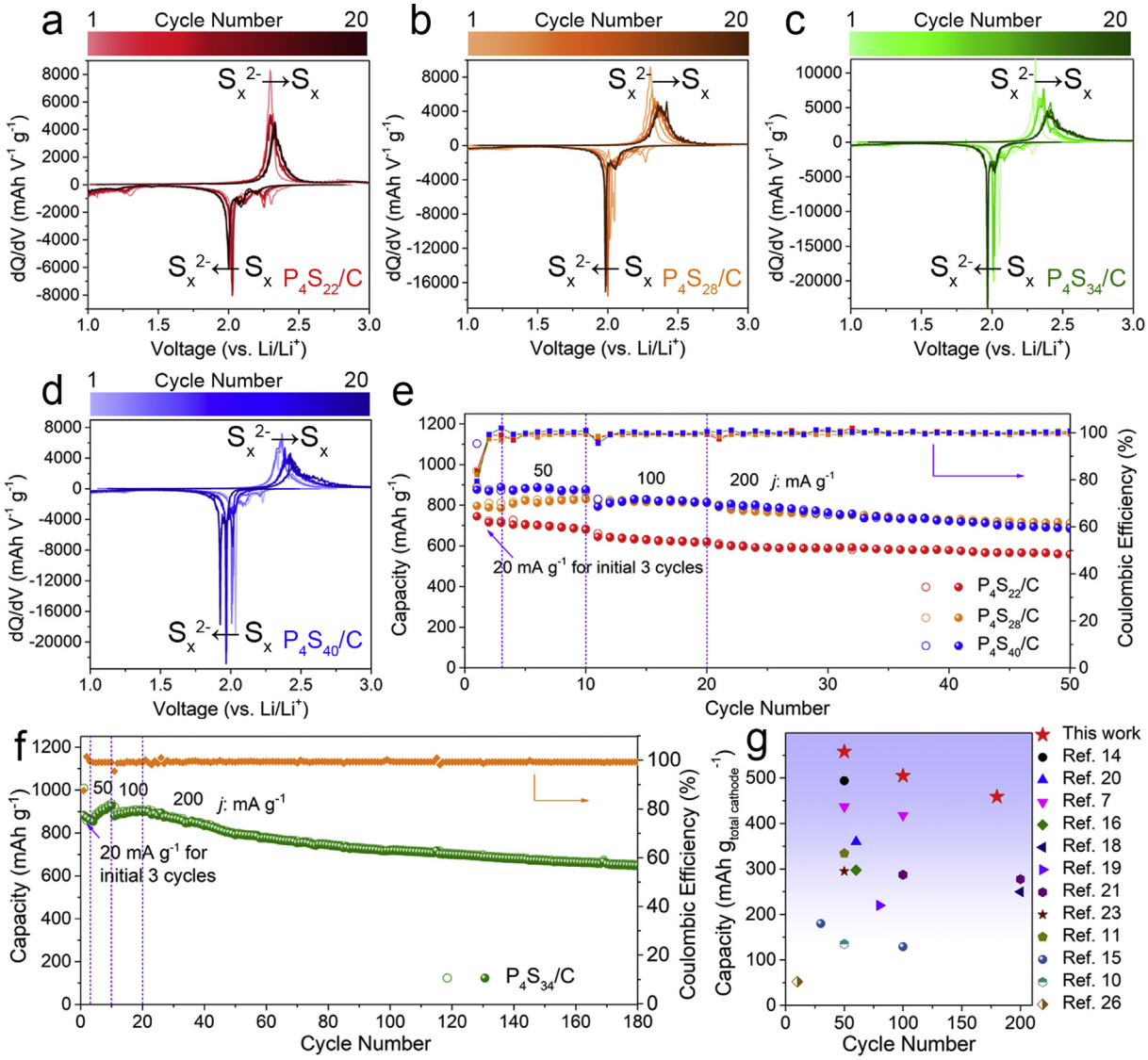

Fig. 6. Electrochemical performance of P_4S_{10+n}/C cathodes. (a–d) dQ/dV curves of P_4S_{10+n}/C cathodes, (e,f) Cycling performance of P_4S_{10+n}/C cathodes at different current densities in sulfide ASSLSBs. (g) Summary of reported capacities based on total weight of cathode composites (active material/SSE/C) in ASSLSBs [7,9–11,14–16,18–21,23,26].

performance, with a high reversible capacity of 655 mAh g^{-1} remained after 180 cycles (Fig. 6f). Based on the proposed electrochemical reaction, the theoretical volume changes of the P_4S_{10+n} cathodes are ranging from 32% to 63%, which are much lower than that of 87% for sulfur cathode. The capacity decay of the P_4S_{10+n}/C cathodes should due to the volume change during lithiation/delithiation process and the possible intercepted ionic or electronic pathways within the cathodes. Although the capacity based on P_4S_{10+n} is not as high as those of S or Li_2S cathodes in ASSLSBs, the capacities based on the total weight of cathode composites are the highest among the reported ASSLSBs as shown in Fig. 6g since no additional solid electrolytes need to be added in cathode composites [7,9–11,14–16,18–21,23,26]. The impressive reversible capacity along with the relatively stable cycling performance for those P_4S_{10+n} molecules as active cathode materials in ASSLSBs can be attributed to (i) the *in-situ* formation of the ionic conductive Li–P–S component together with the sulfur redox components, (ii) uniform distribution of the *in-situ* formed Li–P–S species at nanoscale to facilitate fast sulfur redox for good electrochemical performance. Benefitting from the fact that no SSE additives, the active content within the cathode composite is highly improved to 70 wt%, ensuring higher energy density of the assembled ASSLSBs. More importantly, the electrochemical behavior of active P_4S_{10+n} cathodes can be presented, getting rid of the influence of extrinsic SSEs.

3. Conclusion

In summary, we have successfully demonstrated that the *in-situ* spontaneous formation of highly ionic conductive Li–P–S components during lithiation/delithiation is the key to achieve reversible P_4S_{10+n}/C cathodes free of solid electrolyte additives. Multiple analyses using synchrotron XANES, Raman, and XPS confirm the formation of highly ionic conductive Li_3PS_4 together with a small amount of $Li_4P_2S_6$ species during the initial lithiation process. Subsequently, the uniform formation of the conductive Li–P–S network is maintained to ensure feasible Li^+ migration within the cathode as well as high reversible capacity and good cycling stability of P_4S_{10+n}/C cathodes in ASSLSBs, though the Li–P–S species also partially exhibit reduction/oxidation. Thus, active P_4S_{10+n} content can be as high as 70 wt%. Moreover, the ASSLSBs with P_4S_{34}/C cathode display good cycling performance over 180 cycles. The present study presents a successful example and provides a viable avenue for generating ionic conductive components from the electrode itself to minimize interfacial resistance, facilitate fast Li^+ migration, and getting rid of the influence of SSE decomposition.

Declaration of competing interest

The authors declare that they have no known competing financial interests or personal relationships that could have appeared to influence the work reported in this paper.

CRediT authorship contribution statement

Xiaona Li: Conceptualization, Investigation, Data curation, Writing - original draft. **Jianwen Liang:** Conceptualization, Investigation, Data curation, Writing - original draft. **Mohammad Norouzi Banis:** Investigation, Writing - review & editing. **Jing Luo:** Writing - review & editing. **Changhong Wang:** Investigation, Writing - review & editing. **Weihan Li:** Investigation, Writing - review & editing. **Xia Li:** Writing - review & editing. **Qian Sun:** Writing - review & editing. **Yongfeng Hu:** Formal analysis, Writing - review & editing. **Qunfeng Xiao:** Formal analysis, Writing - review & editing. **Tsun-Kong Sham:** Data curation, Writing - review & editing. **Li Zhang:** Resources, Writing - review & editing. **Shangqian Zhao:** Resources, Writing - review & editing. **Shigang Lu:** Resources, Writing - review & editing. **Huan Huang:** Resources, Writing - review & editing. **Ruying Li:** Resources, Writing - review & editing. **Xueliang Sun:** Supervision, Writing - review & editing.

Acknowledgements

Xiaona Li and Jianwen Liang contributed equally to this work. This research was supported by Natural Sciences and Engineering Research Council of Canada, GLABAT Solid-State Battery Inc., Canada Research Chair Program (CRC), Canada Foundation for Innovation, Ontario Research Fund, the Canada Light Source at University of Saskatchewan (CLS), Canada Mitacs fellow, and University of Western Ontario.

Appendix A. Supplementary data

Supplementary data to this article can be found online at https://doi.org/10.1016/j.ensm.2020.03.014.

References

[1] Y. Kato, S. Hori, T. Saito, K. Suzuki, M. Hirayama, A. Mitsui, M. Yonemura, H. Iba, R. Kanno, Nat. Energy 1 (2016), 16030.
[2] J. Janek, W.G. Zeier, Energy 500 (2016) 300.
[3] N. Kamaya, K. Homma, Y. Yamakawa, M. Hirayama, R. Kanno, M. Yonemura, T. Kamiyama, Y. Kato, S. Hama, K. Kawamoto, Nat. Mater. 10 (2011) 682–686.
[4] M.A. Kraft, S. Ohno, T. Zinkevich, R. Koerver, S.P. Culver, T. Fuchs, A. Senyshyn, S. Indris, B.J. Morgan, W.G. Zeier, J. Am. Chem. Soc. 140 (2018) 16330–16339.
[5] P. Adeli, J.D. Bazak, K.H. Park, I. Kochetkov, A. Huq, G.R. Goward, L.F. Nazar, Angew. Chem. Int. Ed. 58 (2019) 8681–8686.
[6] L. Zhou, A. Assoud, Q. Zhang, X. Wu, L.F. Nazar, J. Am. Chem. Soc. 141 (2019) 19002–19013.
[7] H. Yan, H. Wang, D. Wang, X. Li, Z. Gong, Y. Yang, Nano Lett. 19 (2019) 3280–3287.
[8] A.M. Nolan, Y. Zhu, X. He, Q. Bai, Y. Mo, Joule 2 (2018) 2016–2046.
[9] Z. Lin, Z. Liu, N.J. Dudney, C. Liang, ACS Nano 7 (2013) 2829–2833.
[10] K. Suzuki, N. Mashimo, Y. Ikeda, T. Yokoi, M. Hirayama, R. Kanno, ACS Appl. Energy Mater. 1 (2018) 2373–2377.
[11] S. Wang, Y. Zhang, X. Zhang, T. Liu, Y.-H. Lin, Y. Shen, L. Li, C.-W. Nan, ACS Appl. Mater. Interfaces 10 (2018) 42279–42285.
[12] C. Yu, S. Ganapathy, N.J. de Klerk, I. Roslon, E.R. van Eck, A.P. Kentgens, M. Wagemaker, J. Am. Chem. Soc. 138 (2016) 11192–11201.
[13] X. Li, J. Liang, X. Li, C. Wang, J. Luo, R. Li, X. Sun, Energy Environ. Sci. 11 (2018) 2828–2832.
[14] F. Han, J. Yue, X. Fan, T. Gao, C. Luo, Z. Ma, L. Suo, C. Wang, Nano Lett. 16 (2016) 4521–4527.
[15] X. Yao, N. Huang, F. Han, Q. Zhang, H. Wan, J.P. Mwizerwa, C. Wang, X. Xu, Adv. Energy Mater. 7 (2017), 1602923.
[16] R. Xu, Z. Wu, S. Zhang, X. Wang, Y. Xia, X. Xia, X. Huang, J. Tu, Chem. Eru. J. 23 (2017) 13950–13956.
[17] M. Nagao, A. Hayashi, M. Tatsumisago, Electrochim. Acta 56 (2011) 6055–6059.
[18] L.-P. Hou, H. Yuan, C.-Z. Zhao, L. Xu, G.-L. Zhu, H.-X. Nan, X.-B. Cheng, Q.-B. Liu, C.-X. He, J.-Q. Huang, Energy Stor. Mater. 25 (2020) 436–442.
[19] M. Shin, A.A. Gewirth, Adv. Energy Mater. 9 (2019), 1900938.
[20] R.-c. Xu, X.-h. Xia, S.-h. Li, S.-z. Zhang, X.-l. Wang, J.-p. Tu, J. Mater. Chem. 5 (2017) 6310–6317.
[21] Y. Zhang, T. Liu, Q. Zhang, X. Zhang, S. Wang, X. Wang, L. Li, L.-Z. Fan, C.-W. Nan, Y. Shen, J. Mater. Chem. 6 (2018) 23345–23356.
[22] Q. Han, X. Li, X. Shi, H. Zhang, D. Song, F. Ding, L. Zhang, J. Mater. Chem. 7 (2019) 3895–3902.
[23] J. Yi, L. Chen, Y. Liu, H. Geng, L.-Z. Fan, ACS Appl. Mater. Interfaces 11 (2019) 36774–36781.
[24] N.H. Phuc, M. Takaki, H. Muto, M. Reiko, H. Kazuhiro, A. Matsuda, ACS Appl. Energy Mater. 3 (2020) 1569–1573.
[25] Q. Zhang, N. Huang, Z. Huang, L. Cai, J. Wu, X. Yao, J. Energy Chem. 40 (2020) 151–155.
[26] K. Suzuki, M. Tateishi, M. Nagao, Y. Imade, T. Yokoi, M. Hirayama, T. Tatsumi, R. Kanno, J. Electrochem. Soc. 164 (2017) A6178–A6183.
[27] C. Lin, X. Zhu, J. Feng, C. Wu, S. Hu, J. Peng, Y. Guo, L. Peng, J. Zhao, J. Huang, J. Am. Chem. Soc. 135 (2013) 5144–5151.
[28] A.J. Vaccaro, T. Palanisamy, R. Kerr, J. Maloy, Solid State Ionics 2 (1981) 337–340.
[29] J.M. Whiteley, S. Hafner, S.S. Han, S.C. Kim, V.-D. Le, C. Ban, Y.H. Kim, K.H. Oh, S.-H. Lee, J. Mater. Chem. 5 (2017) 15661–15668.
[30] K. Nagao, Y. Nagata, A. Sakuda, A. Hayashi, M. Tatsumisago, MRS Adv 3 (2018) 1319–1327.
[31] Y. Nagata, K. Nagao, M. Deguchi, A. Sakuda, A. Hayashi, H. Tsukasaki, S. Mori, M. Tatsumisago, Chem. Mater. 30 (2018) 6998–7004.
[32] X. Li, J. Liang, Y. Lu, Z. Hou, Q. Cheng, Y. Zhu, Y. Qian, Angew. Chem. Int. Ed. 56 (2017) 2937–2941.
[33] C. Dietrich, R. Koerver, M.W. Gaultois, G. Kieslich, G. Cibin, J. Janek, W.G. Zeier, Phys. Chem. Chem. Phys. 20 (2018) 20088–20095.
[34] F. Guillou, K. Ollefs, F. Wilhelm, A. Rogalev, A. Yaresko, H. Yibole, N. van Dijk, E. Brück, Phys. Rev. B 92 (2015), 224427.
[35] J. Monnier, D. Vantelon, S. Reguer, P. Dillmann, J. Anal. At. Spectrom. 26 (2011) 885–891.
[36] M.E. Fleet, Can. Mineral. 43 (2005) 1811–1838.

[37] J.M. Whiteley, S. Hafner, S.S. Han, S.C. Kim, K.H. Oh, S.H. Lee, Adv. Energy Mater. 6 (2016), 1600495.
[38] T. Hakari, M. Deguchi, K. Mitsuhara, T. Ohta, K. Saito, Y. Orikasa, Y. Uchimoto, Y. Kowada, A. Hayashi, M. Tatsumisago, Chem. Mater. 29 (2017) 4768–4774.
[39] K. Suzuki, D. Kato, K. Hara, T.-a. Yano, M. Hirayama, M. Hara, R. Kanno, Electrochemistry 86 (2018) 1–5.
[40] M. Tachez, J.-P. Malugani, R. Mercier, G. Robert, Solid State Ionics 14 (1984) 181–185.
[41] Y. Onodera, K. Mori, T. Otomo, A.C. Hannon, M. Sugiyama, T. Fukunaga, IOP Conference Series: Materials Science and Engineering, vol. 18, IOP Publishing, 2011, 022012.
[42] K. Mathew, C. Zheng, D. Winston, C. Chen, A. Dozier, J.J. Rehr, S.P. Ong, K.A. Persson, Sci. data 5 (2018), 180151.
[43] W.D. Richards, L.J. Miara, Y. Wang, J.C. Kim, G. Ceder, Chem. Mater. 28 (2015) 266–273.
[44] R. Koerver, F. Walther, I. Aygün, J. Sann, C. Dietrich, W.G. Zeier, J. Janek, J. Mater. Chem. 5 (2017) 22750–22760.
[45] F. Han, T. Gao, Y. Zhu, K.J. Gaskell, C. Wang, Adv. Mater. 27 (2015) 3473–3483.
[46] D.H. Tan, E.A. Wu, H. Nguyen, Z. Chen, M.A. Marple, J.-M. Doux, X. Wang, H. Yang, A. Banerjee, Y.S. Meng, ACS Energy Lett 4 (2019) 2418–2427.
[47] S. Ohno, R. Koerver, G. Dewald, C. Rosenbach, P. Titscher, D. Steckermeier, A. Kwade, J.r. Janek, W.G. Zeier, Chem. Mater. 31 (2019) 2930–2940.